Full Matrix Capture and the Total Focusing Imaging Algorithm Using Laser Induced Ultrasonic Phased Arrays

Theodosia Stratoudaki[1, 2, a)], Matt Clark[2, b)], and Paul D. Wilcox[1, c)]

[1]*Department of Mechanical Engineering, University of Bristol, University Walk, Bristol, UK*
[2] *Department of Electrical and Electronic Engineering, Faculty of Engineering, University of Nottingham.*

[a)]Corresponding author: t.stratoudaki@physics.org
[b)]matt.clark@nottingham.ac.uk
[c)]p.wilcox@bristol.ac.uk

Abstract. Laser ultrasonics is a technique where lasers are used for the generation and detection of ultrasound instead of conventional piezoelectric transducers. The technique is broadband, non-contact, and couplant free, suitable for large stand-off distances, inspection of components of complex geometries and hazardous environments. In this paper, array imaging is presented by obtaining the full matrix of all possible laser generation, laser detection combinations in the array (Full Matrix Capture), at the nondestructive, thermoelastic regime. An advanced imaging technique developed for conventional ultrasonic transducers, the Total Focusing Method (TFM), is adapted for laser ultrasonics and then applied to the captured data, focusing at each point of the reconstruction area. In this way, the beamforming and steering of the ultrasound is done during the post processing. A 1-D laser induced ultrasonic phased array is synthesized with significantly improved spatial resolution and defect detectability. In this study, shear waves are used for the imaging, since they are more efficiently produced than longitudinal waves in the nondestructive, thermoelastic regime. Experimental results are presented from nondestructive, laser ultrasonic inspection of aluminum samples with side drilled holes and slots at depths varying between 5 and 20mm from the surface.

INTRODUCTION

Laser ultrasonics is a technique where lasers are used for the generation and detection of ultrasound instead of the conventional piezoelectric transducers [1, 2]. The light of a pulsed laser is focused onto the surface of the component to be tested and is absorbed. In metals, the absorption of light happens at the electromagnetic skin depth, which is of the order of a few nm. Thermal diffusion further buries the heated volume to a total of around one micron deep [3]. The absorbed light heats up the irradiated component causing it to expand rapidly, at times that are compared to the rise time of the laser pulse (nanoseconds duration) [4]. This fast, thermo-elastic expansion is the source of the generated ultrasonic wave. The wave then travels through the component and is detected optically, usually by some type of laser interferometer [5]. Laser ultrasonics has several advantages over conventional ultrasonic methods: it is a non contact and couplant free technique, making it suitable for places with limited access [6], hazardous environments [7] and inspection of geometrically complex components [8]. It is also a broadband technique and all modes of ultrasonic waves (e.g. longitudinal, shear, surface waves) are excited.

The use of ultrasonic phased arrays has had a major impact on science, medicine and society, over the past 60 years. During the last decade, there has been a rapid increase in the use of ultrasonic arrays for NDT inspection. A conventional ultrasonic array is made of several ultrasonic transducer elements which can be addressed individually to transmit and receive ultrasonic signals. A phased array can control the directivity and focus of the ultrasound by varying the time delay between the firings of the array elements. The benefits of phased arrays are increased image

43rd Annual Review of Progress in Quantitative Nondestructive Evaluation, Volume 36
AIP Conf. Proc. 1806, 020022-1–020022-9; doi: 10.1063/1.4974563
Published by AIP Publishing. 978-0-7354-1474-7/$30.00

quality and flexibility regarding the range of different inspections (e.g. plane, focused, steered) that can be done from a single location of the array.

Laser induced ultrasonic arrays have been proposed using spatial or temporal modification of the laser beam, or both. Using spatial modification, some of the authors of the present article, have shown successful control of focusing and steering of surface acoustic waves and longitudinal waves [9–11]. Regarding temporal modification of the laser beam, two methods of phased arrays using laser ultrasonics have been proposed in the past: using a single laser source with multiple optical delays and using multiple laser sources. The first method uses a single laser source which is then split and delivered to the target following a range of optical delay paths to achieve the desired time delay. This can be achieved by using multiple optical fibers of variable length [12–16], or a White cell optical delay cavity system [17]. The second method uses an array of laser cavities, fired at the desired time delay [18–20]. Both these methods are expensive in terms of hardware.

An alternative philosophy to array imaging is to perform the imaging in post processing. Previous authors have used the synthetic aperture focusing technique (SAFT) with laser ultrasonics to improve detectability and enhance imaging [21, 22], mainly in the destructive, ablation regime. The authors of the present paper have recently demonstrated [23] Laser Induced Phased Array (LIPA) imaging in post processing, by obtaining the full matrix of all possible transmitter receiver combinations in the array, at the non-destructive, thermoelastic regime. This data acquisition method is known as the Full Matrix Capture (FMC) [24, 25]. A major benefit of this method is that now a whole range of imaging algorithms is possible to be applied to the same data set, in post processing. For laser ultrasonics in particular, the advantage is that array configurations can now be synthesized without the need of complicated optical setups, optical fibers or use of multiple laser beams and without being limited by the physical constraints (e.g. restrictions on the number of array elements) that come with these setups. The present paper presents optimizations to the technique, by introducing apodization terms, in the TFM algorithm. The result is improved signal-to-noise (SNR), hence better defect identification.

BACKGROUND

Laser Based Ultrasound

Ultrasound is generated when the light emitted by a pulsed laser is absorbed by the material. In the low laser power thermoelastic regime there is no damage of the material and the process is non-destructive. The laser beam incident to the sample locally heats its surface and causes it to expand rapidly at times that are comparable to the rise time of the laser pulse which, for the cases considered here, is in the order of 10 ns. As the laser energy is absorbed in a layer much thinner than the ultrasonic wavelength (a few nanometers in aluminum), the bandwidth of the generated wave depends on the temporal characteristics of the laser pulse and is broadband. Longitudinal, shear and surface acoustic waves are generated. For a point source center of expansion, the angular dependence of the amplitude of the longitudinal and the shear waves are given respectively by [4]:

$$G_L(\theta) \propto \frac{\sin\theta \sin 2\theta (\kappa^2 - \sin^2\theta)^{1/2}}{2\sin\theta \sin 2\theta (\kappa^2 - \sin^2\theta)^{1/2} + (\kappa^2 - 2\sin^2\theta)^2} \tag{1}$$

$$G_T(\theta) \propto \frac{\sin 2\theta \cos 2\theta}{\cos^2 2\theta + 2\sin\theta \sin 2\theta (\kappa^{-2} - \sin^2\theta)^{1/2}} \tag{2}$$

where θ is the observation angle with respect to the surface normal and $\kappa=c_L/c_T$, with c_L and c_T the acoustic velocities of the longitudinal and the shear wave respectively. It has been shown [26] that the directivities of the longitudinal and shear waves for a line source, similar to the one used in this study, are the same as those for a point source. In the case of aluminum, the directivity pattern of the longitudinal waves [19] has its maximum at θ=64^o and for shear waves [19, 26] the maximum is at θ=30^o.

Scanning the detection beam creates an array of detectors. The detector used in the work presented here, is sensitive to the out-of-plane ultrasonic component. The sensitivity of the detector to longitudinal and shear waves as a function of incident wave angle, is given, respectively, by [27]:

$$D_L(\theta) \propto \frac{\cos\theta(\kappa^2 - 2\sin^2\theta)}{F_0(\sin\theta)} \tag{3}$$

$$D_T(\theta) \propto \frac{\sin 2\theta(\kappa^2 \sin^2\theta - 1)}{F_0(\kappa\sin\theta)} \tag{4}$$

$$\text{where } F(\xi) = (2\xi^2 - \kappa^2)^2 - 4\xi^2(\xi^2 - 1)^{1/2}(\xi^2 - \kappa^2)^{1/2} \tag{5}$$

Eq. (3) and Eq. (4) are actually the relations for the radial (compressional) and tangential (shear) components respectively, of an excited wave due to an out-of-plane point load on the surface. By reciprocity, these should be proportional to the out-of-plane surface displacement as a function of incident wave angle.

Full Matrix Capture (FMC) and Total Focusing Method (TFM)

The FMC is a data acquisition method developed for conventional ultrasonic arrays. In this method, the waveform from every possible combination of transducer/receiver of an n element array is captured and forms an $n \times n$ matrix, the full matrix. The FMC had to be adapted to data acquired from laser sources and the approach taken here is shown in Fig. 1, as well as a representation of the full matrix. The beam of the generation laser was focused onto a line at the surface of the sample, along the y-axis and the beam of the detection laser was focused onto a spot. The laser beams were scanned in such a way along the x-axis (see section "Experimental Setup") that the collected data correspond to those of a linear array with equi-spaced elements.

Because the generation and detection angular sensitivities are different, it is not readily apparent how this will affect the imaging performance of the system. For this reason, a forward model is desirable to predict the FMC data set, $h_{gd}(t)$ (where the indices g and d refer to ultrasonic generation and detection positions respectively). The model employed is a ray-based model that simulates the response of the system to one or more small targets. In the case of multiple targets, only first-order scattering is considered, hence the response of the system is simply the superposition of its response to each target, individually. Each target generates four separate responses corresponding to the four possible combinations of generated mode and detected mode (longitudinal-longitudinal, longitudinal-shear, shear-longitudinal and shear-shear). Again, these are treated separately and superposed. In the frequency, ω, domain, the response to the j^{th} target for shear generated and detected mode can be written as:

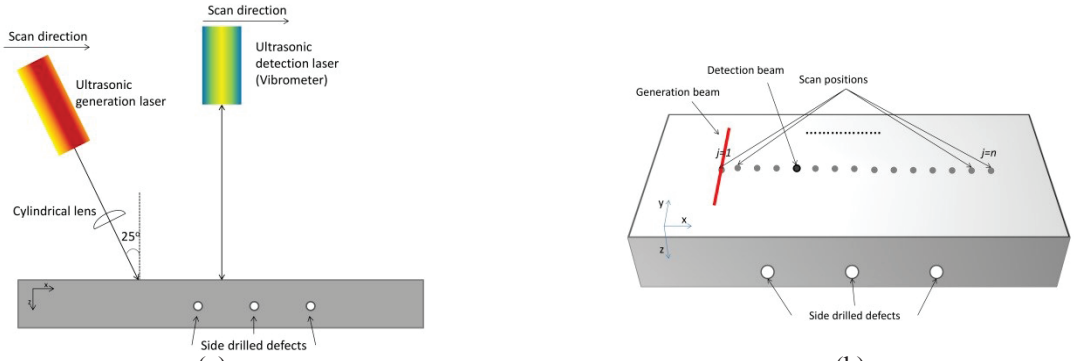

FIGURE 1. Experimental setup, side (a) and top (b) view. (c) The full matrix composed from all signals (s_{gd}).

$$H_{gdj}(\omega) = \frac{G_T(\theta_{gj}) D_T(\theta_{dj})}{(|\mathbf{d}_{gj}||\mathbf{d}_{dj}|)^{1/2}} A_j(\theta_{gj}, \theta_{dj}, \omega) \exp\left[-i\omega \left(\frac{|\mathbf{d}_{gj}| + |\mathbf{d}_{dj}|}{c_T} \right) \right] \quad (6)$$

where θ_{gj} and θ_{dj} are the angles (relative to the surface normal) of the rays between the generation and detection positions and the target, $\mathbf{d}_{gj}$ and $\mathbf{d}_{dj}$ are the corresponding path lengths and $A_j(\theta_{gj};\theta_{dj}, \omega)$ is the angular-dependent response or scattering matrix [28] of the target. The above expression allows the response to any defect to be simulated, subject to the constraint that the generation and detection points must be in the far-field of the defect.

TFM is an algorithm that can only be performed using FMC. It has been shown [24] that the TFM gives significantly improved resolution and SNR compared to swept aperture plane and focused B-scans. In addition, the TFM image extends beyond the edge of the array, increasing the probability of locating defects in these locations.

In TFM, the first step is to discretize the target region (in the x, z plane) into a grid. The signals from all elements in the array are then summed to synthesize a focus at every point in the grid [24]. The intensity of the image, $I(\mathbf{r})$ at any point in the scan is given by [24]:

$$I(\mathbf{r}) = \sum_{g=1}^{n} \sum_{d=1}^{n} Z_g(\mathbf{r}) Z_d(\mathbf{r}) s_{gd}(t_{gd}(\mathbf{r})) \quad (7)$$

where $s_{gd}(t)$ are the digitally filtered time-traces of the raw signals collected during the experiment (see section "Results"). The time delay term (t_{gd}) equals:

$$t_{gd}(\mathbf{r}) = \frac{d_g(\mathbf{r}) + d_d(\mathbf{r})}{c_T} \quad (8)$$

where $d_g(\mathbf{r})$ and $d_d(\mathbf{r})$ are the distances associated with the generation and detection ray-paths. Z_g and Z_d are apodization coefficients. The noise present in experimental FMC data is dominated by incoherent noise that is of uniform RMS amplitude in all signals. In order to maximize the SNR of the TFM image, the optimum apodization is therefore a matched filter that weights each time-trace contribution according to the expected signal amplitude of a scatterer. Without prior knowledge of the type of scatterers to be detected, the most appropriate assumption is that $A_j(\theta_{gj}, \theta_{dj}, \omega)=1$ and the apodization coefficients are then given by:

$$Z_g(\mathbf{r}) = \frac{G_T(\theta_g(\mathbf{r}))}{\left[d_g(\mathbf{r})\right]^{1/2}} \quad (9)$$

$$Z_d(\mathbf{r}) = \frac{D_T(\theta_d(\mathbf{r}))}{\left[d_d(\mathbf{r})\right]^{1/2}} \quad (10)$$

The response model described previously can be used to simulate the FMC data and resultant TFM image from any configuration of suitable scatterers in order to provide a direct comparison with experimental results. The response model can also be combined with the TFM description to produce what is defined as a sensitivity image, E(r), that describes the amplitude expected from a perfect point target (i.e. one where $A_j(\theta_{gj}, \theta_{dj}, \omega)=1$) as a function of position $\mathbf{r}$. The inverse Fourier transform of the Eq. (6) for the shear-shear mode combination is:

$$h_{gd} = \frac{G_T(\theta_g(\mathbf{r})) D_T(\theta_d(\mathbf{r}))}{\left[d_g(\mathbf{r}) d_d(\mathbf{r})\right]^{1/2}} \delta\left(t - \frac{d_g(\mathbf{r}) + d_d(\mathbf{r})}{c_T} \right) \quad (11)$$

Hence the sensitivity image is:

$$E(\mathbf{r}) = \left| \sum_{g=1}^{n} \sum_{d=1}^{n} Z_g(\mathbf{r}) Z_d(\mathbf{r}) \frac{G_T(\theta_g(\mathbf{r})) D_T(\theta_d(\mathbf{r}))}{\left[d_g(\mathbf{r}) d_d(\mathbf{r}) \right]^{1/2}} \right|$$
$$= \left| \sum_{g=1}^{n} Z_g(\mathbf{r}) \frac{G_T(\theta_g(\mathbf{r}))}{\left[d_g(\mathbf{r}) \right]^{1/2}} \sum_{d=1}^{n} Z_d(\mathbf{r}) \frac{D_T(\theta_d(\mathbf{r}))}{\left[d_d(\mathbf{r}) \right]^{1/2}} \right| \quad (12)$$

EXPERIMENTAL RESULTS

Experimental Setup

Two samples were used in this study. Each one was a 90 × 20 × 50 mm block of aluminum and five side drilled holes or slots were imaged in each sample. The schematic of the samples used is shown in Fig. 2 and the characteristics of the imaged reflectors are given in Table 1.

The experimental setup is depicted in Fig. 1(a) and (b). The generation laser was a Nd:YVO pulsed laser with pulse rise time of 1 ns and 1064 nm wavelength. Its repetition rate was 5 kHz and the average power 680 mW, as measured in front of the sample, corresponding to 136 mJ per pulse. The laser beam was focused by means of a cylindrical lens, to a line of 5 mm length in the y-direction (i.e. perpendicular to the imaging plane) and 0.2 mm width in the x-direction. The incidence angle was 25° with respect to the normal to the sample surface. This was purely to facilitate the scanning of the generating and detecting laser beams and only has a minor effect on the directivity pattern of the ultrasonic waves.

A Polytech vibrometer (OFV-534 head with OFV-5000 controller) was used to detect the ultrasonic signal, which was measuring the out-of-plane displacement. The light of the 633nm HeNe laser that it uses was focused to a 0.04mm diameter spot and was aligned with the middle of the generation line source with an angle of incidence 0° with respect to the normal.

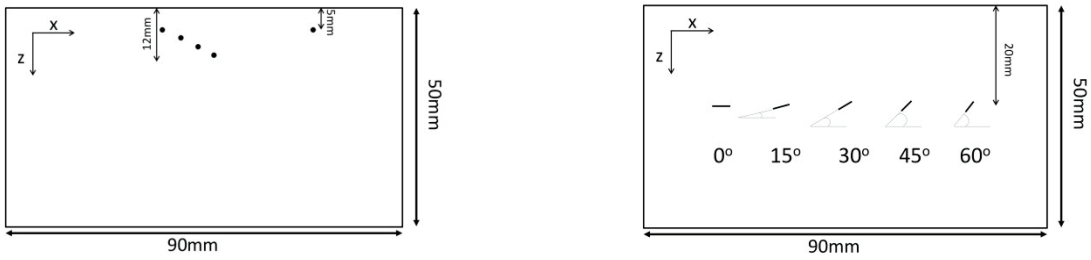

FIGURE 2. Schematic diagram of sample 1 (a) and sample 2 (b), side views. Sample 1 has through holes and sample 2 has through slots of orientations ranging from 0°-60°.

TABLE 1. Details of side drilled holes and slots in experimental samples.

Sample	Reflector	Depth from surface (mm)	Type	Dimensions (mm)	Orientation (°)
1	1	5	hole	ø1.2	N/A
	2	8	hole	ø1.2	N/A
	3	10	hole	ø1.2	N/A
	4	12	hole	ø1.2	N/A
	5	5	hole	ø1.2	N/A
2	1	20	slot	3x1	0
	2	20	slot	3x1	15
	3	20	slot	3x1	30
	4	20	slot	3x1	45
	5	20	slot	3x1	60

During the data acquisition for the FMC, a 1-D LIPA was synthesized. In the case of sample 1, it was a 89 element array with element spacing of 155μm and in the case of sample 2, it was a 161 element array with element spacing of 155μm. To synthesize the LIPA in each case, the sample remained stationary, throughout the experiment, while the detection and the generation laser beams were scanned in turns. The detection laser was scanned across all consecutive array element positions, while the generation laser remained focused at one position. Then the generation laser beam was moved, irradiating another element position and the detection laser was scanned again across all element positions [Fig. 1(b)]. The bandwidth of the vibrometer is from low MHz to 24 MHz, with a flat frequency response across its bandwidth. Each captured waveform was averaged 500 times.

Results

A 1 MHz high pass, analog filter was applied during the data collection, to reduce some of the signal noise, without loss of useful information. Digital filtering of the signal was performed in order to maximize the SNR. The inspection frequency was tuned by means of a Gaussian filter with 100% bandwidth, at -40 dB and was applied to the raw time-traces during the post processing. The digital filters applied had various central frequency values, as specified in each case. The shear wave was chosen to image the defects as the contribution of the longitudinal wave is small in the thermoelastic regime, in metals [4]. The shear wave velocity of 3100m/s was used in Eq. (8). The directivity of the shear wave shows a max. at 30^o and there was enough out-of-plane component to be detected by the vibrometer. The surface acoustic wave was present in all data and can be seen present at the TFM images at the surface, extending to a crosstalk region of depth up to 5mm.

Figure 3(a) shows the TFM image from sample 1, using 8 MHz digital filter. Five defects are very well resolved, at depths 5 mm (reflector 1 at x=-17 mm and reflector 5 at x=13 mm from the center of the array), 8 mm (at x=-14 mm from the center of the array), 10 mm (at x=-10 mm from the center of the array) and 12 mm (at x=-6 mm from the center of the array). The level of intensity of the TFM images (in this and in all subsequent images) in decibel units, is defined as:

$$I_{dB} = 20\log_{10}\frac{I(\mathbf{r})}{I_{\max}} \tag{13}$$

where $I(\mathbf{r})$ is defined in Eq. (7) and I_{max} has a single value in each image, corresponding to the maximum intensity of the image at depths>5 mm. This means that images are normalized to the largest defect response, rather than the very high amplitude surface wave artifacts present at shallower depths. Figure 3(b) shows the sensitivity image ($E(\mathbf{r})$), as described by Eq. (12). It can be seen that the sensitivity is not uniform. As a result, $I(\mathbf{r})$ (shown in Fig. 3(a)) has uniform noise but non-uniform sensitivity. To account for this effect, the normalized image ($N(\mathbf{r})=I(\mathbf{r})/E(\mathbf{r})$) is shown in Fig. 3(c). $N(\mathbf{r})$ has non-uniform noise (the noise in areas of weak signal is amplified), but uniform sensitivity.

Figure 4(a) shows the TFM image from sample 2, using 8 MHz digital filter. The five defects can be seen with high spatial resolution. Figure 4(b) shows the sensitivity image ($E(\mathbf{r})$) and once again, it is non-uniform. Figure 4(c) shows the normalized image of the experimental data, where the sensitivity is uniform.

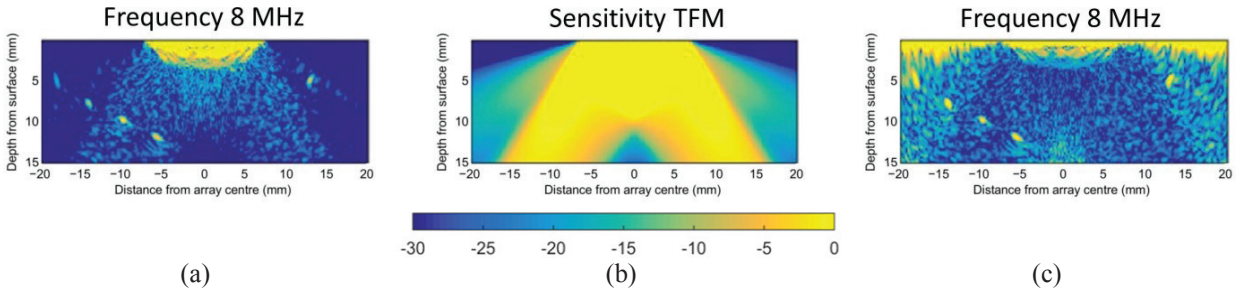

FIGURE 3. (a) TFM image of sample 1 using experimental data from an array of 89 elements and 500 averages. (b) the sensitivity image and (c) the normalized TFM image of the experimental data, shown in (a), over the sensitivity, shown in (b). A filter of 8MHz was applied in post processing and the dynamic range of the image is 30dB.

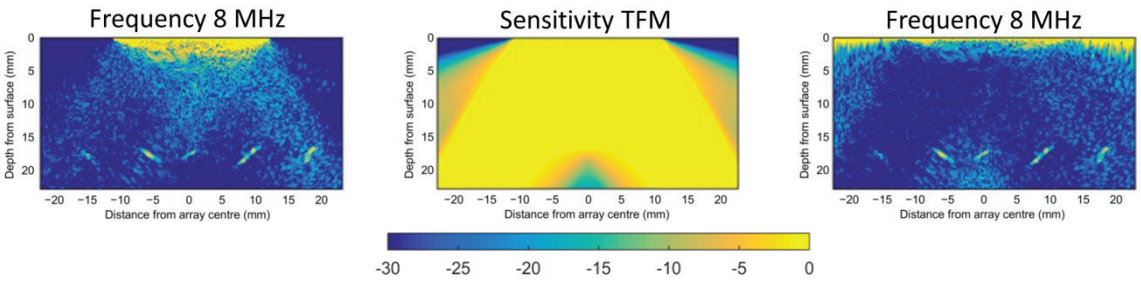

(a) (b) (c)

FIGURE 4. (a) TFM image of sample 2 using experimental data from an array of 161 elements and 500 averages. b) the sensitivity image and (c) the normalized TFM image of the experimental data, shown in (a), over the sensitivity, shown in (b). A filter of 8MHz was applied in post processing and the dynamic range of the image is 30dB.

DISCUSSION

A limitation of the FMC is the need to acquire $n \times n$ signals. The procedure becomes even more time consuming when averaging of multiple signals is needed. This was the case in the work presented here, as laser ultrasonic generation at the thermoelastic regime generally produces weak signals. At the moment, the data acquisition speed is 1.5 points per second, which means in practice that it takes under 5 minutes to capture the full matrix of a 20 element array and 90 minutes for an 89 element array. The theoretical maximum speed of FMC (v_{max}) is determined by the minimum time per FMC frame ($T_{min} = m \times n^2 \times 1/f$, where m is the number of averages and f is the laser repetition rate), which is the time taken to acquire one complete full matrix. In the results presented, each waveform was averaged 500 times and the repetition rate of the laser was 5 kHz, corresponding to $T_{min} \approx 13$ min., for an 89 element array. It can be seen that with the current experimental setup, data acquisition is 7 times slower than the theoretical limit and this is currently limited by the mechanical scanning and the data acquisition system. The system is being re-designed to address these issues. However, T_{min} can be further improved and the FMC using LIPAs can become faster and several improvements are proposed below to address this challenge.

Improve the Signal to Noise Ratio

For a laser ultrasonics system using an interferometer, the SNR, is related to the surface displacement (δ), the optical power reaching the detector (P_D) and the bandwidth (B_D) of the detection system, via the following proportionality [29]:

$$SNR \propto \sqrt{n^2 m} \cdot \delta \cdot \frac{P_D}{B_D} \tag{14}$$

The surface displacement, at the thermoelastic regime, increases linearly with increasing the generation laser power, P_G [30], and, for the experiments presented here, P_G is already set at the limit before damage occurs (damage threshold in aluminum is ~150 kW/mm^2 [19]). Another option is to increase the reflected light power, P_D. Given a certain surface finish of the tested sample, increasing the power of the detection laser will improve the SNR [31]. The vibrometer used in this study is of very low laser power (<1mW) and a higher power laser would be more appropriate. In order to give a realistic example of what the effect of some of the suggested improvements would be to the system, assuming a detection laser of 100 mW power, and full light return from the sample, an increase of SNR by a factor of 10 compared to the existing setup, would be observed. This would lower the number of averages by a factor of 102 and averaging of only a few pulses would be required. If no averaging were required, the theoretical limit for the FMC, would be $n^2 \times 1/f$, limited only by the repetition rate of the generation laser. It is noted here that the repetition rate of the generation laser is ultimately limited by the minimum time required between successive firings to ensure that the reverberations from the previous cycle have sufficiently decayed before the next. In the case of LIPAs, this quantity sets the limit to the maximum repetition rate (f_{max}) of the generation laser that can be used. As an example and based on values of attenuation in aluminum published in the literature [32], for an aluminum sample with same physical dimensions as the one in this study, the f_{max} is approx. 15 kHz, corresponding to three times faster data acquisition than the current rate.

Another option that would reduce the number of averages is to modulate the spatial intensity distribution of the generation laser beam, using Hadamard multiplexing, which has been shown to improve the SNR [33]. In [33], an improvement of SNR by 2.8 was observed. This is equivalent to the SNR improvement obtained by increasing the number of averages by a factor of $2.8^2 = 8$. A similar improvement to our currently used system would reduce the number of averages from 500 to 60, increasing the data acquisition speed by a factor of 8 as well.

CONCLUSIONS

The results presented here give an experimental demonstration of the benefits of using the FMC data acquisition method and the TFM as a post processing algorithm in laser ultrasonics. The beamforming and steering of the ultrasound is done during the post processing, resulting in a laser induced phased array with significantly improved spatial resolution and defect detectability. The technique is non-contact and non-destructive and would be attractive for applications such as inspection of carbon fiber composites or welded parts in microelectronics, performing NDT in hazardous environments or at the production line. The system can be easily fiber coupled to access difficult to reach places, and can accommodate complex geometries. The lasers themselves are relatively small and portable. The use of optics makes the array elements easy to manipulate: change spot size and scan.

The FMC allows post processing in a range of different algorithms, including the TFM, which can only be performed when the full matrix is known. In addition, the TFM allows the detection of defects outside the array aperture and improves the spatial resolution and SNR. In the present paper, apodization has been applied at the imaging algorithm: the contribution of each captured waveform is weighted by the transmit and receive directivity functions at each image point. If noise in the original waveforms is uniform then this apodization maximizes SNR at each point in image

Laser ultrasonics is a broadband technique, allowing the results to be post processed in a range of frequencies, a significant advantage over the conventional transducers. The choice of frequency can be adjusted according to the expected defect size, depth and material properties. In [23], it was shown that there is an optimization to reach between overall SNR and lateral resolution. This information can be used to optimize the speed of the data acquisition process, as lower frequencies mean larger array spacing (i.e. fewer array elements for the same size aperture) during data collection.

The main concern regarding FMC coupled with laser ultrasonics is the time for data acquisition. Improvements are proposed in this paper that address making data acquisition faster. The following is a realistic example of what the effect of some of the suggested system improvements would be to the theoretical speed limit: assuming a detection laser of 100 mW power, and full light return from the sample, an increase of SNR by a factor of 10 compared to the existing setup, would be observed, lowering the number of averages by a factor of 102. As a result, only few or no averaging would be required. If no averaging were required then, assuming an ultrasonic generation laser with repetition rate of 15 kHz and an array of n=89 elements, the theoretical limit for the FMC, would be ($T_{min} = n^2 \times 1/f$) 500 ms per frame. Based on the suggested developments and a re-design of the experimental system, it is expected that the theoretical speed limit for LIPAs using FMC will be approached within the next few years.

REFERENCES

1. S. J. Davies, C. Edwards, G. S. Taylor, and S. B. Palmer, J. Phys. D: Appl. Phys. **26**, 329-348 (1993).
2. C. B. Scruby and L. E. Drain, *Laser Ultrasonics, Techniques and Applications* (Adam Hilger, Bristol, 1990).
3. K. L. Telschow and R. J. Conant, J. Acoust. Soc. Am. **88**, 1494-1502 (1990).
4. L.R.F. Rose, J. Acoust. Soc. Am. **75**, 723-732 (1984).
5. J. P. Monchalin, IEEE Trans. Ultrason., Ferroelectr., Freq. Control **33,** 485–499 (1986).
6. L. S. Wang, J. S. Steckenrider and J. D. Achenbach, "A fiber-based laser ultrasonic system for remote inspection of limited access components", in *Review of Progress in Quantitative Nondestructive Evaluation,* eds. D. O. Thompson and D. E. Chimenti (Plenum Press, NY), **16**, 507-514 (1997).
7. M. Dubois, M. Militzer, A. Moreau, J. F. Bussiere, Scripta Materialia **42**, 867-874 (2000).
8. K. R. Yawn, M. A. Osterkamp, D. Kaiser, C. Barina, "Improved laser ultrasonic systems for industry", in *Review of Progress in Quantitative Nondestructive Evaluation*, eds. D. E. Chimenti, L. J. Bond, and D. O. Thompson, (American Institute of Physics 1581, Melville, NY), **33**, 397-404 (2014).
9. M. Clark, S. D. Sharples, and M. G. Somekh, J. Acoust. Soc. Am. **107**, 3179–3185 (2000).
10. S. D. Sharples, M. Clark, and M. G. Somekh, Ultrasonics **41**, 295–299 (2003).

11. T. Stratoudaki, M. Clark, and M. G. Somekh, "Cheap optical transducers (CHOTS) for generation and detection of longitudinal waves", in *IEEE International Ultrasonics Symposium – 2012*, IEEE International Ultrasonics Symposium (IEEE, New York, NY, 2012), pp. 961–964.
12. A. J. A. Bruinsma and J. A. Vogel, Appl. Optics **27**, 4690–4695 (1988).
13. J. Jarzynski and Y. H. Berthelot, J. Acoust. Soc. Am. **8**, 158–162 (1989).
14. S. N. Hopko, I. C. Ume, and D. S. Erdahl, J. Manuf. Sci. E. - T ASME **124**, 351–357 (2002).
15. B. Mi and C. Ume, J. Manuf. Sci. E. - T. ASME **128**, 280–286 (2006).
16. C. Pei, K. Demachi, T. Fukuchi, K. Koyama, and M. Uesaka, J. Appl. Phys. **113**, 163101 (2013).
17. J. S. Steckenrider, T. W. Murray, J. B. D. Jr., and J. W. Wagner, J. Acoust. Soc. Am. **97**, 273–279 (1995).
18. J. T. W. Murray, J. B. Deaton and J. W. Wagner, Ultrasonics **34**, 69–77 (1996).
19. M.-H. Noroy, D. Royer, and M. Fink, J. Acoust. Soc. Am. **94**, 1934–1943 (1993).
20. M.-H. Noroy, D. Royer, and M. Fink, IEEE T. Ultrason. Ferr. **42**, 981–988 (1995).
21. A. Blouin, D. Levesque, C. Neron, D. Drolet, and J.-P. Monchalin, Opt. Express **2**, 531–539 (1998).
22. D. Levesque, A. Blouin, C. Neron, and J.-P. Monchalin, Ultrasonics **40**, 1057-1063 (2002).
23. T. Stratoudaki, M. Clark, P. D. Wilcox, Opt. Express **24**, 21921-21938 (2016).
24. P. D. Wilcox, C. Holmes, B. W. Drinkwater, NDT&E Int. **38**, 701-711 (2005).
25. P. D. Wilcox, C. Holmes, B. W. Drinkwater, Ultrasonics **48**, 636-642 (2008).
26. J.R. Bernstein and J.B. Spicer, J. Acoust. Soc. Am. **107**, 1352-1357 (2000).
27. G. F. Miller and H. Pursey, "The field and radiation impedance of mechanical radiators on the free surface of a semi-infinite isotropic solid," in *Proceedings of the Royal Society of London. Series A*, Mathematical and Physical Sciences 223, (Royal Society, 1954), pp. 521–542.
28. J. Zhang, B. W. Drinkwater, and P. D. Wilcox, IEEE T. Ultrason. Ferr. **55**, 2254–2265 (2008).
29. J. Wagner and J. Spicer, J. Opt. Soc. Am. **4**, 1316–1326 (1987).
30. A. M. Aindow, R. J. Dewhurst, D. A. Hutchins, and S. B. Palmer, J. Acoust. Soc. Am. **69**, 449–455 (1981).
31. J. Wagner, "Breaking the sensitivity barrier: the challenge for laser ultrasonics," in *IEEE 1992 Ultrasonics Symposium*, Proceedings of IEEE 1992 Ultrasonics Symposium 1 and 2, (IEEE, New York, 1992), pp. 791–800.
32. Y.-J. Chen, Mater. Trans. **50**, 2308–2313 (2009).
33. G. Rousseau and A. Blouin, Opt. Express **20**, 25798–25816 (2012).